

RESEARCH ARTICLE | JUNE 06 2025

Viscoelastic flow instability in planar shear flow

Ivan S. Novikau ; Sofia S. Kantorovich ; Sebastian A. Altmeyer  



Physics of Fluids 37, 063109 (2025)

<https://doi.org/10.1063/5.0261021>



Articles You May Be Interested In

Long-term degradation of high molar mass poly(ethylene oxide) in a turbulent pilot-scale pipe flow

Physics of Fluids (February 2023)



Physics of Fluids

Special Topics Open for Submissions

[Learn More](#)



Viscoelastic flow instability in planar shear flow

Cite as: Phys. Fluids **37**, 063109 (2025); doi: [10.1063/5.0261021](https://doi.org/10.1063/5.0261021)

Submitted: 28 January 2025 · Accepted: 21 March 2025 ·

Published Online: 6 June 2025



View Online



Export Citation



CrossMark

Ivan S. Novikau,¹  Sofia S. Kantorovich,¹  and Sebastian A. Altmeyer^{2,a)} 

AFFILIATIONS

¹University of Vienna, Computational and Soft Matter Physics, 1090 Vienna, Austria

²Castelldefels School of Telecom and Aerospace Engineering, Universitat Politècnica de Catalunya, 08034 Barcelona, Spain

^{a)}Author to whom correspondence should be addressed: sebastian.andreas.altmeyer@upc.edu.

URL: <http://www.sebastianaltmeyer.de>

ABSTRACT

We report direct numerical simulations of elastic turbulence in shear-driven flow of a dilute polymer solution within a three-dimensional straight channel. Most existing approaches in the literature employ the Oldroyd-B model or its advanced version, the finite extensible nonlinear elastic model introduced by Peterlin (FENE-P model), for simulation of polymer hydrodynamics, with their limitations of being continuum models. To overcome such restriction, we explicitly model the dilute polymer solution utilizing a classical bead-spring representation for each polymer chain and, therefore, also accounting for spatial variations in polymer concentration. We show that the viscoelastic instability forms in elastic waves and eventually chaotic flow, which persists above the transition with increasing Weissenberg number further into viscoelastic turbulence.

© 2025 Author(s). All article content, except where otherwise noted, is licensed under a Creative Commons Attribution (CC BY) license (<https://creativecommons.org/licenses/by/4.0/>). <https://doi.org/10.1063/5.0261021>

I. INTRODUCTION

To date the transition from laminar flows to instability, turbulence, and chaos is not fully understood and, therefore, is still in the focus of actual research. Even more, discrepancies between experiments, the linear and nonlinear analysis, and the experiments (known as the Sommerfeld paradox¹) The general findings/observations for classical plane Poiseuille flow are as follows: (i) it is linearly unstable for $Re > 5772$,² (ii) it is linearly stable for all Reynolds numbers,³ (iii) in laboratory experiments it undergoes transition to three-dimensional turbulence for Reynolds numbers between 300 and 400; and (iv) nonlinear asymptotic L2-energy-stability⁴ has been proved for Reynolds numbers, Re , below similar values.

While persistent challenges in classical turbulence underscore inertial complexity, modern drag-reduction strategies increasingly modify intrinsic fluid properties. Dissolving polymers into viscous solvents produces viscoelastic solutions that suppress turbulent drag through vortex damping mechanisms leveraged industrially for energy-efficient transport.⁵ However, viscoelasticity introduces elasticity-driven instabilities absent in Newtonian systems: polymer stretching generates non-inertial turbulence precursors that demand revised stability analysis frameworks.

Most common viscoelastic instabilities occur due to sufficiently strong forcing applied to the flow of polymer solutions or strong coupling between the (viscous) fluid flow and the material's elasticity. To

date, there are enormous amounts of flows that have been demonstrated to be elastically unstable. In their recent work, Datta *et al.*⁶ provide an excellent overview of a purely elastic flow instability map (PEFIM, Fig. 2) of the different viscoelastic flow instabilities that have been documented so far. This work bridges the gap between viscometric and shear-dominated regimes, offering insights into how elastic stresses reshape stability thresholds—a critical step toward reconciling polymer-modified flows with classical turbulence paradigms.

In the simulation of polymers in hydrodynamic media, most existing approaches in the literature employ the Oldroyd-B model or its advanced version, the FENE-P model, which treats polymers as an effective field.^{7–9} In contrast, our method explicitly models the dilute polymer solution using a classical bead-spring representation for each polymer chain.¹⁰ This approach overcomes significant limitations of continuum models, such as accounting for spatial variations in polymer concentration, as observed experimentally under shear conditions,¹¹ and directly resolving chain dynamics, including the tumbling of individual polymer chains,¹² along with excluded volume interactions between monomers. Building on our approach, we present direct numerical simulations of elastic turbulence in shear-driven flow of the dilute polymer solution. This study focuses on the modeling of a polymer fluid within a three-dimensional straight channel defined by Cartesian coordinates (Fig. 1): x (streamwise), y (spanwise), and z (wall-normal). The channel is confined between parallel plates fully

filled with the fluid. The shear rate $\dot{\gamma}$ is induced by the movement of the top plate along the x axis at a velocity \vec{u}_0 .

Periodic boundary conditions are applied in both the x - and y -directions. We characterize the flow using the longest polymeric relaxation time, τ_R , to define the Weissenberg number, $Wi = \tau_R \dot{\gamma}$, which indicates the balance between elastic and viscous forces. The governing system requires solving the Navier–Stokes equations (NS) using the lattice Boltzmann method (LB), coupled with the Langevin equation solved through molecular dynamics (MD). Further details on the method are provided in Sec. II below, followed by Sec. III, where we introduce the studied viscoelastic instability, examine its dynamics and inner structure, and analyze how other simulation parameters affect the instability. τ_R calculations are in the Appendix.

II. MODEL AND METHODS

The fluid motion in our simulations is governed by NS,

$$\begin{aligned} \frac{\partial \rho}{\partial t} + \nabla \cdot (\rho \vec{u}) &= 0, \\ \frac{\partial (\rho \vec{u})}{\partial t} + \nabla \cdot (\rho \vec{u} \vec{u}) &= -\nabla p + \nabla \cdot \left[\mu \left(\nabla \vec{u} + (\nabla \vec{u})^T \right) \right] + \vec{F}, \end{aligned} \quad (1)$$

where ρ is the fluid density, \vec{u} is the velocity field, p is the pressure, μ is the dynamic viscosity, and \vec{F} represents external forces.

NS are approximated by the LB scheme,^{13,14} which solves a discretized lattice Boltzmann equation (LBE) whose hydrodynamic moments recover NS in the continuum limit. The governing LBE reads

$$f_i(\vec{x} + \vec{c}_i \Delta t, t + \Delta t) = f_i(\vec{x}, t) + \Delta t \Omega_i(\vec{x}, t). \quad (2)$$

Here, $f_i(\vec{x}, t)$ denotes the density of fluid particles with discrete velocity \vec{c}_i at position \vec{x} and time t ; Δt is the time step. The collision operator $\Omega_i(\vec{x}, t)$, typically modeled via the Bhatnagar–Gross–Krook approximation as

$$\Omega_i(\vec{x}, t) = -\frac{1}{\tau} (f_i(\vec{x}, t) - f_i^{\text{eq}}(\vec{x}, t)), \quad (3)$$

drives the system toward equilibrium. The relaxation time τ controls viscosity and $f_i^{\text{eq}}(\vec{x}, t)$ corresponds to the Maxwell–Boltzmann distribution. Our implementation uses the D3Q19 lattice model with 19 predetermined velocity vectors \vec{c}_i in a 3D grid. The macroscopic velocity field $\vec{u}(\vec{x}, t)$ emerges from the lattice dynamics through

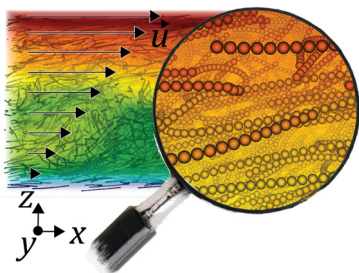


FIG. 1. Snapshot of the simulated system with overlaid arrows indicating the direction and magnitude of flow, while the multicolored background represents velocity magnitude gradients. The zoomed-in section reveals polymer chains.

$$\vec{u}(\vec{x}, t) = \frac{1}{\rho(\vec{x}, t)} \sum_i \vec{c}_i f_i(\vec{x}, t), \quad (4)$$

linking the discrete LBE solution to the continuous NS.^{15,16}

To couple the fluid with polymers, we compute the $\vec{u}(\vec{r}_i(t), t)$ at i th monomer position, $\vec{r}_i(t)$, via trilinear interpolation across neighboring grid nodes (see Fig. 2). A friction force,

$$\vec{F}_{i,\text{frict}} = -\zeta (\vec{v}_i(t) - \vec{u}(\vec{r}_i(t), t)), \quad (5)$$

where ζ is the friction coefficient and $\vec{v}_i(t)$ is the monomer velocity, acts on both the monomers and the fluid in opposite directions, thereby mediating hydrodynamic interactions between monomers.

Polymer dynamics evolves through MD algorithm. Each i th monomer obeys the Langevin equation with a modified friction term according to the coupling mechanism mentioned above,

$$M_i \frac{d\vec{v}_i(t)}{dt} = \vec{F}_i + \vec{F}_{i,\text{frict}} + \sqrt{2\zeta k_B T} \eta_i(t), \quad (6)$$

where M_i is the monomer mass, \vec{F}_i includes all deterministic interparticle forces, T is the temperature, k_B is the Boltzmann constant, and $\eta_i(t)$ is a delta-correlated stationary Gaussian process with zero-mean; consequently, the last term corresponds to the “thermal” force.

Simulations are carried out in a simulation unit (SU) system, with the monomer serving as the reference length scale, set to a dimensionless diameter of $\sigma = 1$. Table I provides the simulation units (SUs) and their equivalents in the International System of Units (SI). The chosen monomer size reasonably estimates the persistence length of hyaluronic acid (HA),¹⁷ while hydrated HA approaches the density of water.¹⁸ Energy, time, and mass units are chosen to balance stable and time-effective simulation of HA in water at room temperature.

The simulations are conducted in a rectangular box with dimensions of $314\sigma \times 157\sigma \times 157\sigma$, and the LB lattice constant is set to $a_{\text{grid}} = 1\sigma$. The system evolves with a time step of $\delta t = 0.0001$, with the LB fluid field updated at each MD step. Shear flow is induced by the constant motion of the upper wall with a no-slip boundary condition.

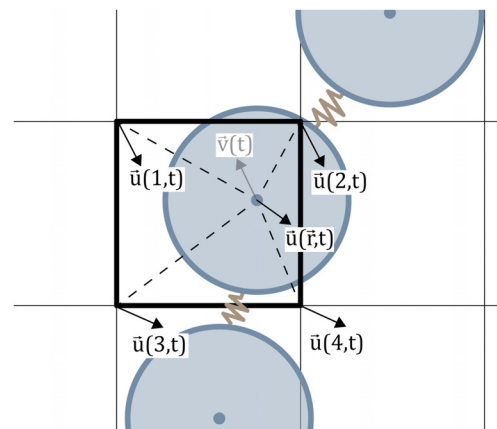


FIG. 2. A simplified 2D scheme in which coupling is ensured by the friction force in Eq. (5), driven by the difference between the monomer velocity $\vec{v}(t)$ and fluid velocity $\vec{u}(\vec{r}, t)$, later is interpolated from grid velocities $\vec{u}(1\dots 4, t)$. Blue circles represent monomers connected by brown springs. Multimedia available online.

TABLE I. System parameters in SI and their corresponding values in simulation units.

System:	SI units	Sim. units
Energy unit	179 k_B 298.15 K	1 (E)
Time unit	3.40×10^{-11} s	1 (t)
Mass unit	5.35×10^{-23} kg	1 (m)
Distance unit	4 nm	1 (x) = 1 σ
Kin. viscosity	8.92×10^{-7} m ² s ⁻¹	1.90 (x) ² (t) ⁻¹
Solvent density	0.997×10^3 kg ² m ⁻³	1.19 (m) (x) ⁻³
Polymer density	0.997×10^3 kg ² m ⁻³	1.19 (m) (x) ⁻³

Steric repulsion between polymer beads and between the channel walls and polymer beads is modeled using the Weeks–Chandler–Andersen (WCA) potential, a shifted and truncated version of the Lennard-Jones (LJ) potential,¹⁹

$$\beta U_{WCA}(r) = \begin{cases} 4 \left[\left(\frac{\sigma}{r} \right)^{12} - \left(\frac{\sigma}{r} \right)^6 \right] + 1, & r \leq 2^{1/6}, \\ 0, & r > 2^{1/6}, \end{cases} \quad (7)$$

where r represents the distance between the centers of two interacting beads measured in units of σ , $\beta = 1/(k_B T)$ is the Boltzmann factor.

Polymer chains contain 15–50 beads, linked by stiff harmonic springs between adjacent beads. The harmonic potential is defined as

$$U_h(r) = \frac{1}{2} K (r - \sigma)^2. \quad (8)$$

In this context, the elastic constant is $K = 30 \times 10^4$.

Alternatively, we explored connecting the beads using finitely extensible nonlinear elastic (FENE) springs.¹⁰ The FENE potential is defined as

$$U_{FENE}(r) = -\frac{1}{2} \varepsilon_f r_f^2 \ln \left[1 - \left(\frac{r}{r_f} \right)^2 \right], \quad (9)$$

with the bond rigidity $\varepsilon_f = 30$ and the maximum bond extension $r_f = 1.5$. In this setup, polymers are allowed to break if the distance between two beads exceeds 1.5σ , resulting in the elimination of the corresponding FENE bond. This approach revealed similar pulsating instabilities as observed with harmonic springs. However, these simulations proved to be less stable, and resolving the detailed dynamics of polymer breakage lies beyond the scope of this study.

Overall, the described approach is implemented in the ESPResSo simulation package, version 4.2.²⁰

III. RESULTS AND DISCUSSION

A. Instability

Our numerical simulations indicate that as the Wi increases, corresponding to a higher shear rate, the shear flow becomes unstable. At low Wi , we observe a simple shear flow that matches the analytic solution $\vec{u}(x, y, z) = (\dot{\gamma}z, 0, 0)$. To examine the transition, we define an order parameter based on the turbulent kinetic energy (TKE). Specifically, the instability dynamics are characterized by the TKE

evolution: in each point of the hydrodynamic field, we calculate the TKE as

$$\text{TKE}_{yz}(x, y, z) = \frac{1}{2} \left(\overline{(u'_y)^2} + \overline{(u'_z)^2} \right), \quad (10)$$

where the fluctuating velocity components are given by

$$\overline{(u')^2} = \frac{1}{N_{\text{steps}}} \sum_{i=1}^{N_{\text{steps}}} (u_i - \bar{u})^2. \quad (11)$$

Summing $\text{TKE}_{yz}(x, y, z)$ over the entire channel volume yields the order parameter TKE_{yz} , shown in Fig. 3 as a function of Wi . By isolating the crossflow component of turbulent kinetic energy, TKE_{yz} , which accounts solely for fluctuations in the y and z directions, we derived a more refined order parameter.

A clear transition from the laminar base flow ($\text{TKE}_{yz} = 0$) to the emergence of a secondary flow ($\text{TKE}_{yz} > 0$) is observed as the shear rate $\dot{\gamma}$ increases beyond a critical value of $Wi_c = 1.65 \times 10^3$. The transition is marked by a sharp increase in the order parameter, scaling as $(Wi - Wi_c)^\xi$ with $\xi = 0.65$. The continuous increase in the order parameter with Wi suggests a supercritical instability accompanied by an increase in flow resistance. Similar behavior was previously observed in the context of Taylor–Couette flow.^{21,22}

We examine the Reynolds number range in simulations using the standard definition $Re = u_0 L / \nu$, where L is the channel width and ν is the kinematic viscosity. Data in Fig. 3 span $Re = 486$ – 9322 , with $Re_{\text{critical}} \approx 5037$. Prior work indicates laminar-to-turbulent transitions in microchannels occur at $Re > 2000$.²³ Therefore, our simulated instability arises in a regime where elastic (polymer-driven) and inertial (viscous/inertial-driven) turbulence coexist.

B. Dynamics of the instability

After identifying the emergence of instability, we proceed to investigate the dynamics of the flow field beyond the elastic instability in more detail. Therefore, the insights in Fig. 3(b) illustrate the evolution of TKE_{yz} across the instability. It clearly shows that the flow becomes stronger and more irregular, also including velocity bursts after crossing the elastic instability.

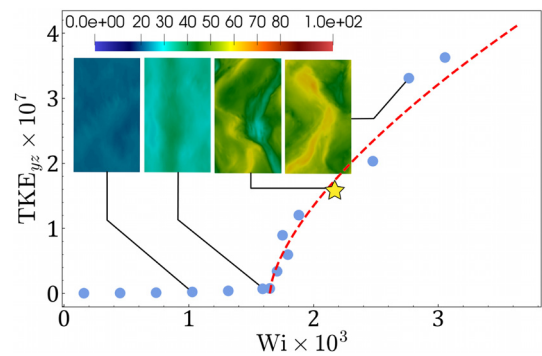


FIG. 3. Bifurcation diagram of the elastic instability: order parameter TKE_{yz} as a function of Wi . The red dashed line indicates the fitted scaling law $(Wi - Wi_c)^\xi$ with $Wi_c = 1.65 \times 10^3$ and $\xi = 0.65$, beyond the elastic instability. Insets illustrate color-coded velocity field slices in the mid-channel xy -plane for different Wi as indicated. The star denotes the configuration shown in Fig. 4.

To study the system's dynamics, we compute the dynamic structure factor (SF).^{24–26} The SF is the space- and time-Fourier transform of the density–density correlation function, quantifying how density fluctuations evolve over time and space. It links spatial scales to temporal behavior, revealing the system's excitation spectrum. The dynamic SF is defined as

$$S(\vec{q}(\theta_n), t_1, t_2) = \sum_{i=0}^{N_p-1} e^{i\vec{q}(\theta_n) \cdot [\vec{r}_i(t_1) - \vec{r}_i(t_2)]}. \quad (12)$$

The wave vector $\vec{q}(\theta_n) = (0, q_0 \cos(\theta_n), q_0 \sin(\theta_n))$ is defined with $\theta_n = \frac{2\pi n}{N_q}$ for $n = 0, 1, \dots, N_q - 1$, where $N_q = 128$. This represents the number of q -vectors in a ring within the y - z plane, orthogonal to the polymer flow. Historically, SF emerged as a mathematical description of how materials (e.g., flowing polymers) scatter incident radiation, later linked to $\vec{q}(\theta_n)$, which probes density fluctuations at a wavelength $\sim 2\pi/q_0$ in directions perpendicular to the flow. $q_0 = 0.03$ effectively probes simulated instability and aligns with the rule of thumb $q_0 \approx 2\pi/L$. $\vec{r}_i(t_1) - \vec{r}_i(t_2)$ is the displacement of the i th monomer between times t_1 and t_2 , and N_p is the total number of monomers. Averaging over all θ_n and monomers yields the averaged dynamic SF, plotted in Fig. 4(b).

$$\overline{S(q_0, t_1, t_2)} = \frac{1}{N_p N_q} \sum_{n=0}^{N_q-1} |S(\vec{q}(\theta_n), t_1, t_2)|. \quad (13)$$

This measures the correlation between structures formed in the system at timesteps t_1 and t_2 . For instance, the dark square-like structure in the bottom-left corner of Fig. 4(b) represents the initial alignment of polymer chains along the flow direction, before the onset of instability (i.e., the laminar base flow). This is followed by a pulsating jet-like structure along the diagonal, characterized by alternating wider and narrower

regions, which reflect the dynamics of the instability. Larger fluctuation sizes indicate more stable structures, while narrower fluctuations correspond to more chaotic regimes. The peaks and troughs in the TKE_{yz} time series shown in Fig. 4(a) strongly correlate with the fluctuation widths. For clarity, Fig. 4(c) shows snapshots of narrower chaotic regions (left) and a more stable state close to laminar flow (right).

The overall dynamics of the instability are cyclic and can be divided into three main stages as shown in Fig. 2 (Multimedia available online): (1) initial alignment of polymer chains along the flow direction, with wave-like perturbations forming in the yz -plane; (2) the formed wave reaches the channel height and chokes, disrupting the uniformity of the flow profile in the xz -plane; and (3) the flow profile becomes more chaotic, with vortices forming and quickly dissipating.

C. Evolution of the instability

To further understand the instability, its internal structure is examined. Figure 5(a) displays the colored vorticity field and gray polymer chains, revealing the formation of a large vortex and its interaction with the polymer chains, particularly their stretching and alignment with the local flow, framing the vortex. The vortex's orientation is diagonal, implying significant components along all three axes. The inside of the vortex appears sparse, with a higher polymer concentration in the surrounding regions, especially above the vortex.

Another visual confirmation of uneven polymer density is shown in Fig. 5(b). A darker stripe, which lies in the xy -plane and is aligned along the x axis, splits the elongated vortex bodies. Polymer density in the darker stripe is lower than in the surrounding lighter regions, with a V-shaped depletion clearly visible at the top of the snapshot.

The polymers appear bent in snapshots. We calculate the end-to-end distance, r_{ee} , of polymer chains, defined as the absolute value of the vector connecting the first and last monomers, i.e., $\vec{r}_{ee} = \vec{r}_{\text{last}} - \vec{r}_{\text{first}}$. The r_{ee} distribution is plotted as a heatmap for each time step in Fig. 5(c). The heatmap shows an irregular black dashed

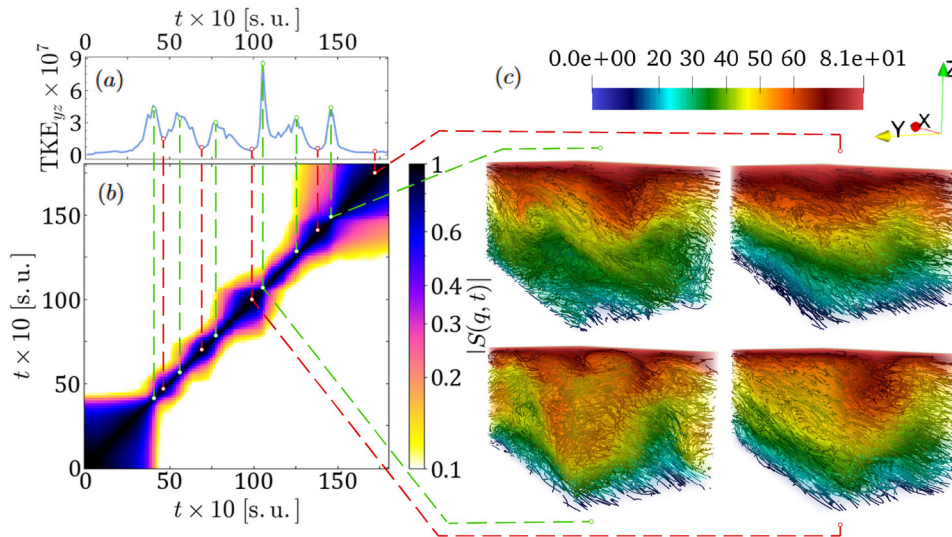


FIG. 4. Supercritical instability at $Wi = 2.19 \times 10^3$ [see star in Fig. 3(b)]. (a) Time series of TKE_{yz} . (b) Dynamic structure factor. (c) Flow pattern snapshots: the two on the left correspond to a more chaotic regime, while the two on the right depict a more stable state close to laminar flow. For more details regarding the dynamics, please see movie_1 (Fig. 2, multimedia available online).

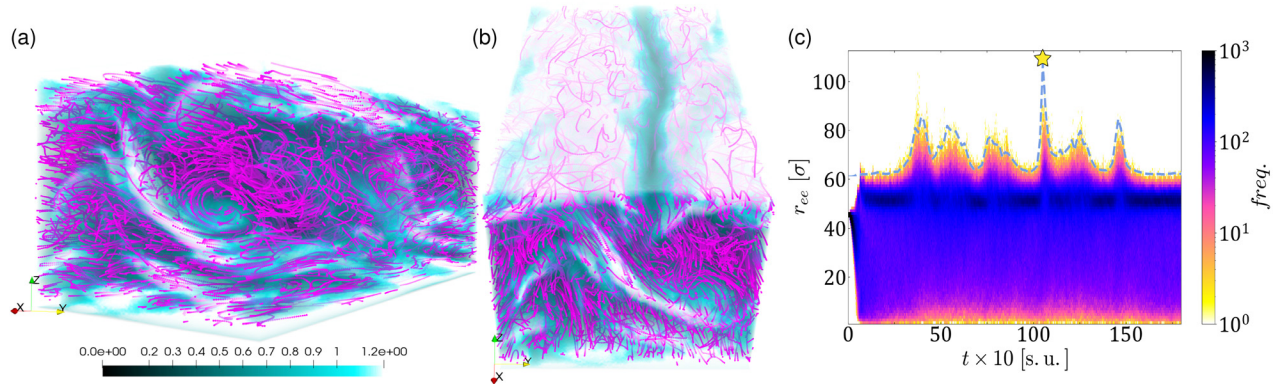


FIG. 5. Inside the instability. (a) and (b) Vorticity field (color-coded) and polymer chains (magenta), showing a large vortex and polymer depletion region. $Wi = 2.19 \times 10^3$. (c) End-to-end distance heatmap over time. Blue dashed line represents the TKE_{yz} time series from Fig. 4(a). Star marks the time step of snapshots (a) and (b).

band around $r_{ee} = 50$, representing the default polymer chain length. Interruptions in the band correspond to peaks, indicating excessive polymer stretching. The blue dashed line on the heatmap, taken from the TKE_{yz} time series [Fig. 4(a)], reveals that peaks in the heatmap coincide with peaks in the TKE_{yz} time series, suggesting that polymer stretching is directly linked to flow instability and vortex formation.

This scenario could potentially lead to polymer chain breakage, with the polymer in turn constraining the vortex and limiting its expansion.

D. Parameter dependence

Further analysis explores how the instability depends on parameters such as polymer chain length, l , and concentration, ϕ_p . Figure 6(a) shows the variation of TKE_{yz} with l , keeping the total number of chains constant. Instability appears beyond the critical chain length at $l_c = 26$ beads. The red dashed line represents the fitted scaling law $(l - l_c)^\xi$ with $\xi = 0.67$. At $l \approx 35$ beads, $TKE_{yz}(l)$ peaks and then decreases with further increases in l , indicating flow stabilization with longer chains. To illustrate the development of the irregular flow pattern after the instability, we present in Fig. 6(b) the time evolution for three selected polymer lengths: immediately after the instability ($l = 27$), at the maximum TKE_{yz} ($l = 35$), and further beyond the instability ($l = 50$). Energy bursts are clearly visible for all polymer lengths; however, close to the instability ($l = 27$), they appear only at the very end of the shown time series. With increasing l , the bursts become more frequent, indicating turbulent dynamics. For larger l , the average amplitude in $TKE_{yz}(l)$ decreases along with lower minima, which suggests greater flow stabilization.

Figures 6(c) and 6(d) illustrate the dependence of TKE_{yz} on ϕ_p at two different fixed chain lengths $l = 30$ and $l = 50$, respectively. The red dashed lines show the fitted scaling law $(\phi_p - \phi_{p,c})^\xi$ with $\xi = 0.70$, where the critical concentration $\phi_{p,c}$ is 0.55% for $l = 30$ and, as extrapolated, 0.13% for $l = 50$. Comparing Figs. 6(c) and 6(d) reveals that instability occurs at significantly lower concentrations for longer chains, consistent with previous experimental findings.²⁷

In Fig. 6(c), TKE_{yz} peaks before declining with further increases in ϕ_p , similar to the behavior observed in Fig. 6(a). This pattern once again suggests flow stabilization at higher polymer concentrations.

Figure 6(e) illustrates the stretching of the polymer bonds. Here, a key idea is that longer polymers tend to be more stretchable. “Mean” and “max” refer to the analysis of bond distances at a given snapshot—either by calculating the average or taking the maximum values among all polymeric chains, which we then average over time regardless of the “mean” or “max.” Furthermore, at $\phi_p = 1.2$, both configurations have the same TKE [Figs. 6(c) and 6(d)], indicating that even at equal TKE, longer chains tend to stretch more.

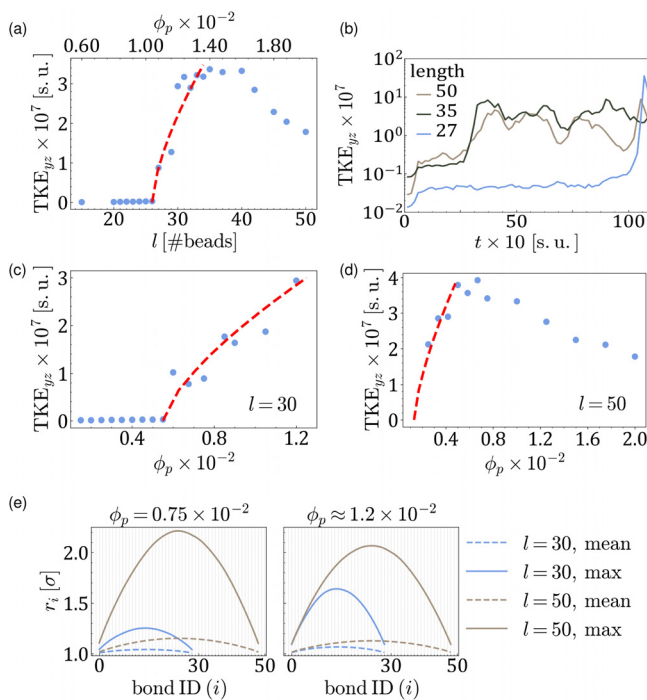


FIG. 6. Effect of other parameters on the instability. (a) Order parameter TKE_{yz} vs chain length l . (b) Time series of TKE_{yz} for different chain lengths [as indicated in (a)] below and above the instability. (c) and (d) Variation of TKE_{yz} with concentration ϕ_p at fixed chain lengths $l = 30$ and $l = 50$, respectively. The red dashed lines indicate the fitted scaling laws beyond the elastic instability: $(l - l_c)^\xi$ with $l_c = 26$, $\xi_1 = 0.67$, and $(\phi_p - \phi_{p,c})^{\xi_2}$ with $\xi_2 = 0.7$. (e) Stretching of polymer bonds (mean and max refer to the analysis of bond distances at a given snapshot, see main text for further explanation).

IV. CONCLUSION

In conclusion, we studied the elastic instability of a dilute polymer solution within a three-dimensional straight channel, using a classical bead-spring representation for each polymer chain to account for spatial variations in polymer concentration and to overcome the limitations of common continuum models (Oldroyd-B, FENE-P). By varying the control parameters—the Weissenberg number, polymer lengths, and concentration—we elucidated the interplay between flow and instability. We characterized the instability dynamics using TKE and used the dynamic structure factor to gain further insight into system dynamics. We observed that peaks and troughs in the TKE time series strongly correlate with fluctuation widths in the dynamic structure factor, suggesting a direct link between polymer stretching, flow instability, and vortex formation. This scenario could potentially lead to polymer chain breakage, with the polymer in turn constraining the vortex and limiting its expansion. Future works will focus on unveiling the exact bifurcation type and seeing if this might give an insight into the polynomial scalings with Wi , length, and concentration.

Getting further insight into the transitional pathway associated with the instability may help to develop control strategies to control transition to turbulence, which would be of special relevance to microfluidic devices.^{28–30}

ACKNOWLEDGMENTS

Computer simulations were performed on the Vienna Scientific Cluster (VSC-5). I.S.N. is grateful to the Doctoral College Advanced Functional Materials (DCAFM) for financial support. This work was supported by the Spanish Government under grants PID2023-150014OB-C21 and PID2023-150029NB-I00.

AUTHOR DECLARATIONS

Conflict of Interest

The authors have no conflicts to disclose.

Author Contributions

Ivan S. Novikau: Conceptualization (equal); Data curation (equal); Formal analysis (equal); Investigation (equal); Methodology (equal); Resources (equal); Software (equal); Validation (equal); Visualization (equal); Writing – original draft (equal); Writing – review & editing (equal). **Sofia S. Kantorovich:** Resources (equal); Writing – review & editing (equal). **Sebastian A. Altmeyer:** Conceptualization (equal); Formal analysis (equal); Investigation (equal); Methodology (equal); Project administration (equal); Supervision (equal); Validation (equal); Writing – original draft (equal); Writing – review & editing (equal).

DATA AVAILABILITY

The data that support the findings of this study are available from the corresponding author upon reasonable request.

APPENDIX: CALCULATION OF THE RELAXATION TIME

To determine the relaxation time τ_R , we analyze the auto-correlation function of the polymer end-to-end vector, \vec{r}_{ee} , under equilibrium conditions (i.e., zero shear rate, $\dot{\gamma} = 0$),

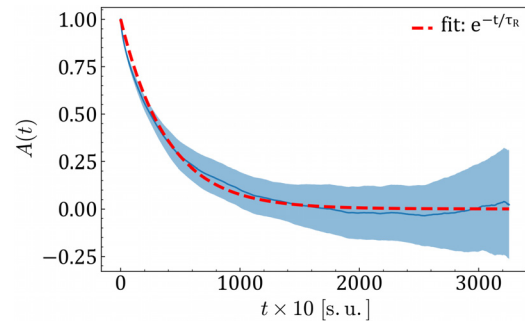


FIG. 7. Relaxation time calculation for a polymer. The red dashed line represents the exponential fit to $A(t)$, and the shaded area indicates ± 0.5 standard deviation. $\tau_R = 4276$ (s.u.).

$$A(t) = \frac{\langle \vec{r}_{ee}(t) \cdot \vec{r}_{ee}(0) \rangle}{\langle \vec{r}_{ee}(0) \cdot \vec{r}_{ee}(0) \rangle}. \quad (\text{A1})$$

The relaxation time τ_R is then extracted by fitting $A(t)$ with an exponential decay function (see Fig. 7): $f(t) = \exp(-t/\tau_R)$, from which we find $\tau_R = 4276$ [s.u.]. The polymer studied consists of a chain length of $l = 50$ beads.

REFERENCES

- ¹A. Sommerfeld, “Ein Beitrag zur hydrodynamischen Erklärung der turbulenten Flüssigkeitsbewegungen,” in *Proceedings of the 4th International Congress of Mathematicians III* (Tipografia della R. Accademia dei Lincei, 1908), pp. 116–124.
- ²S. A. Orszag, “Accurate solution of the Orr-Sommerfeld stability equation,” *J. Fluid Mech.* **50**, 689–703 (1971).
- ³V. A. Romanov, “Stability of plane-parallel Couette flow,” *Funct. Anal. Appl.* **7**, 137–146 (1973).
- ⁴B. Straughan, “The energy method, stability and nonlinear convection,” in *Applied Mathematical Sciences* (Springer-Verlag New York, 2004), Vol. 91.
- ⁵L. Brandfellner, A. Bismarck, and H. W. Müller, “Time for polymers: Onset of drag reduction in the Reynolds–Weissenberg-plane,” *Phys. Fluids* **37**, 035175 (2025).
- ⁶S. S. Datta, A. M. Ardekani, P. E. Arratia, A. N. Beris, I. Bischofberger, G. H. McKinley, J. G. Eggers, J. E. López-Aguilar, S. M. Fielding, A. Frishman, M. D. Graham, J. S. Guasto, S. J. Haward, A. Q. Shen, S. Hormozi, A. Morozov, R. J. Poole, V. Shankar, E. S. G. Shaqfeh, H. Stark, V. Steinberg, G. Subramanian, and H. A. Stone, “Perspectives on viscoelastic flow instabilities and elastic turbulence,” *Phys. Rev. Fluids* **7**, 080701 (2022).
- ⁷H. A. Castillo Sánchez, M. R. Jovanović, S. Kumar, A. Morozov, V. Shankar, G. Subramanian, and H. J. Wilson, “Understanding viscoelastic flow instabilities: Oldroyd-B and beyond,” *J. Non-Newtonian Fluid Mech.* **302**, 104742 (2022).
- ⁸M. Beneitez, J. Page, and R. R. Kerswell, “Polymer diffusive instability leading to elastic turbulence in plane Couette flow,” *Phys. Rev. Fluids* **8**, L101901 (2023).
- ⁹M. Lellep, M. Linkmann, and A. Morozov, “Purely elastic turbulence in pressure-driven channel flows,” *Proc. Natl. Acad. Sci. U. S. A.* **121**, e2318851121 (2024).
- ¹⁰K. Kremer and G. S. Grest, “Dynamics of entangled linear polymer melts: A molecular-dynamics simulation,” *J. Chem. Phys.* **92**, 5057–5086 (1990).
- ¹¹S. Saito and T. Hashimoto, “Critical conditions for structure formation in semidilute polymer solutions induced under continuous shear flow,” *J. Chem. Phys.* **114**, 10531–10543 (2001).
- ¹²C.-C. Huang, G. Sutmann, G. Gompper, and R. G. Winkler, “Tumbling of polymers in semidilute solution under shear flow,” *Europhys. Lett.* **93**, 54004 (2011).
- ¹³I. Pagonabarraga, “Lattice Boltzmann modeling of complex fluids: Colloidal suspensions and fluid mixtures,” in *Novel Methods in Soft Matter Simulations* (Springer, 2004), pp. 279–309.
- ¹⁴B. Dünweg and A. J. C. Ladd, “Lattice Boltzmann simulations of soft matter systems,” in *Advanced Computer Simulation Approaches for Soft Matter Sciences III* (Advances in Polymer Science, 2008).

- ¹⁵S. Succi and S. Succi, "The lattice Boltzmann equation: For complex states of flowing matter," *Numerical Mathematics and Scientific Computation Series* (Oxford University Press, 2018).
- ¹⁶T. Krüger, H. Kusumaatmaja, A. Kuzmin, O. Shardt, G. Silva, and E. Viggen, *The Lattice Boltzmann Method: Principles and Practice, Graduate Texts in Physics* (Springer International Publishing, 2016).
- ¹⁷R. L. Cleland, "The persistence length of hyaluronic acid: An estimate from small-angle X-ray scattering and intrinsic viscosity," *Arch. Biochem. Biophys.* **180**, 57–68 (1977).
- ¹⁸X. Xu, A. K. Jha, D. A. Harrington, M. C. Farach-Carson, and X. Jia, "Hyaluronic acid-based hydrogels: From a natural polysaccharide to complex networks," *Soft Matter* **8**, 3280–3294 (2012).
- ¹⁹J. D. Weeks, D. Chandler, and H. C. Andersen, "Role of repulsive forces in determining the equilibrium structure of simple liquids," *J. Chem. Phys.* **54**, 5237–5247 (1971).
- ²⁰F. Weik, R. Weeber, K. Szuttor, K. Breitsprecher, J. de Graaf, M. Kuron, J. Landsgesell, H. Menke, D. Sean, and C. Holm, "ESPREsSo 4.0—An extensible software package for simulating soft matter systems," *Eur. Phys. J. Spec. Top.* **227**, 1789–1816 (2019).
- ²¹R. van Buel, C. Schaaf, and H. Stark, "Elastic turbulence in two-dimensional Taylor-Couette flows," *Europhys. Lett.* **124**, 14001 (2018).
- ²²L. Corté, P. M. Chaikin, J. P. Gollub, and D. J. Pine, "Random organization in periodically driven systems," *Nat. Phys.* **4**, 420–424 (2008).
- ²³D. Liu and S. V. Garimella, "Investigation of liquid flow in microchannels," *J. Thermophys. Heat Transfer* **18**, 65–72 (2004).
- ²⁴J.-P. Hansen and I. R. McDonald, *Theory of Simple Liquids: With Applications to Soft Matter* (Academic Press, 2013).
- ²⁵L. Van Hove, "Correlations in space and time and born approximation scattering in systems of interacting particles," *Phys. Rev.* **95**, 249–262 (1954).
- ²⁶K. Sturm, "Dynamic structure factor: An introduction," *Z. Naturforsch.* **48**, 233–242 (1993).
- ²⁷S. J. Haward, G. H. McKinley, and A. Q. Shen, "Elastic instabilities in planar elongational flow of monodisperse polymer solutions," *Sci. Rep.* **6**, 33029 (2016).
- ²⁸E. J. Lim, T. J. Ober, J. F. Edd, S. P. Desai, D. Neal, K. W. Bong, P. S. Doyle, G. H. McKinley, and M. Toner, "Inertio-elastic focusing of bioparticles in microchannels at high throughput," *Nat. Commun.* **5**, 4120 (2014).
- ²⁹S. O. Hong, J. J. Cooper-White, and J. M. Kim, "Inertio-elastic mixing in a straight microchannel with side wells," *Appl. Phys. Lett.* **108**, 014103 (2016).
- ³⁰X.-B. Li, F.-C. Li, W.-H. Cai, H. N. Zhang, and J. C. Yang, "Very-low-*Re* chaotic motions of viscoelastic fluid and its unique applications in microfluidic devices: A review," *Exp. Therm. Fluid Sci.* **39**, 1–16 (2012).